JPhys Energy

PURPOSE-LED PUBLISHING™

PAPER • **OPEN ACCESS**

Li$^+$ diffusion in crystalline lithium silicides: influence of extrinsic point defects and structural complexity

To cite this article: Christoph Kirsch *et al* 2026 *J. Phys. Energy* **8** 015004

View the article online for updates and enhancements.

You may also like

- Defect engineering in BiVO$_4$ photoanodes: the synergistic role of nitrogen doping and oxygen vacancy for oxygen evolution reaction
  Qiuhua Liang, Hassan Ouhbi, Nicklas Österbacka et al.
- Metal oxide candidates for thermochemical water splitting obtained with a generative diffusion model
  Matthew D Witman, Reese E Jones, Andrew J E Rowberg et al.
- Hydroxylammonium formate-assisted crystal regulation of -FAPbI$_3$
  Yu-Na Lee, Yu-Na Kim, Hwa-Jin Lee et al.

Your Lab in a Box!

EL-CELL®
electrochemical test equipment

The PAT-Tester-i-16 Multi-Channel Potentiostat for Battery Material Testing!

✓ All-in-One Solution with Integrated Temperature Chamber (+10 to +80 °C)!
No additional devices are required to measure at a stable ambient temperature.

✓ Fully Featured Multi-Channel Potentiostat / Galvanostat / EIS!
Up to 16 independent battery test channels, no multiplexing.

✓ Ideally Suited for High-Precision Coulometry!
Measure with excellent accuracy and signal-to-noise ratio.

✓ Small Footprint, Easy to Setup and Operate!
Cableless connection of 3-electrode battery test cells. Powerful EL-Software included.

Learn more on our product website:
Scan me!

Download the data sheet (PDF):
Scan me!

Or contact us directly:
☎ +49 40 79012-734
✉ sales@el-cell.com
www.el-cell.com

This content was downloaded from IP address 141.48.67.87 on 12/12/2025 at 08:54

IOP Publishing J. Phys. Energy **8** (2026) 015004 https://doi.org/10.1088/2515-7655/ae175e

Journal of Physics: Energy

RECEIVED
16 June 2025

REVISED
7 October 2025

ACCEPTED FOR PUBLICATION
24 October 2025

PUBLISHED
6 November 2025

PAPER

Li^+ diffusion in crystalline lithium silicides: influence of extrinsic point defects and structural complexity

Christoph Kirsch[1], **Christian Dreßler**[2] **and Daniel Sebastiani**[1,*]

[1] Martin-Luther-University Halle-Wittenberg, Institute of Chemistry, Theoretical Chemistry, Von-Danckelmann-Platz 4, 06120 Halle (Saale), Germany
[2] Ilmenau University of Technology, Theoretical Solid State Physics, Weimarer Straße 32, 98693 Ilmenau, Germany
[*] Author to whom any correspondence should be addressed.

E-mail: daniel.sebastiani@chemie.uni-halle.de

Keywords: first principles molecular dynamics simulations, lithium diffusion, lithium–ion batteries, silicon anodes, extrinsic defects, crystal structure complexity

Supplementary material for this article is available online

Abstract

$Li_{15}Si_4$, which forms in Si anodes for Li-ion batteries upon full lithiation, belongs to a class of binary crystalline lithium-silicon compounds Li_xSi_y. In this study, by combining *ab initio* molecular dynamics simulations and nudged elastic band calculations, the impact of isovalent extrinsic point defects on Li diffusion in Li_1Si_1, $Li_{12}Si_7$, $Li_{13}Si_4$, and $Li_{15}Si_4$ is explored through the incorporation of Na and Ge atoms. Since Na interstitials turn out to be unstable, larger elements are identified as substitutional atoms in these compounds. Overall, both cationic and anionic substitution have only minor effects on Li mobility. Energy barriers for Li migration marginally increase near Na and Ge atoms and decrease at larger distances. Na migration energies are approximately 30% higher than those of Li atoms. Moreover, defect formation energies in stoichiometric Li_xSi_y systems are shown to be inversely correlated with crystal structure complexity.

1. Introduction

High-performance energy storage technologies, like advanced rechargeable batteries, are required, for example, for electric vehicles and the efficient use of renewable energies. Lithium-ion batteries (LIBs) have not only been the standard in portable electronics for a long time, but they have also been established in modern electric cars. To facilitate their application in larger-scale energy storage systems, a primary aim is to improve the LIBs' energy density, with research efforts focusing on finding new electrode materials, which is crucial for achieving this enhancement [1, 2].

Silicon is a promising material for high-capacity anodes in next-generation LIBs. When fully lithiated to $Li_{15}Si_4$, Si has a gravimetric energy density of $3579\,\mathrm{mA\,h\,g^{-1}}$ [3], enabling it to store nearly ten times more Li than graphite, the most often commercially used anode material, that has an energy density of $372\,\mathrm{mA\,h\,g^{-1}}$ for LiC_6 [4]. However, mechanical failures in silicon anodes notably reduce their cyclability, which imposes a significant barrier to the replacement of graphite in LIBs. This issue arises from the substantial structural and volumetric changes that occur during the charging/discharging process. For instance, crystalline Si experiences approximately a 380% volume increase when forming $Li_{15}Si_4$ [3]. In contrast, only a 13% volume expansion to LiC_6 and minor structural changes result from reversible intercalation of Li ions between graphite layers during lithiation. Consequently, only minimal capacity loss is caused by multiple lithiation/delithiation cycles in graphite anodes [4, 5]. To address the difficulties in cycling silicon anodes, researchers are extensively investigating the use of silicon nanostructures and composite materials. Hollow, porous, or yolk-shell nanoarchitectures accommodate volume expansion through internal voids, and in composites, soft conductive matrices, such as carbon, buffer these volume changes and maintain electronic and ionic contact [3].

Electrochemical lithiation of a crystalline silicon electrode at room temperature generates amorphous Li_xSi [6], crystallizing to $Li_{15}Si_4$ at $x = 3.75$, beyond which no additional lithium can be inserted [7, 8]. Upon delithiation of $Li_{15}Si_4$, the material reverts to amorphous Li_xSi and ultimately becomes amorphous Si [7, 8]. Although $Li_{15}Si_4$ is the only crystalline Li_xSi_y compound identified during the cycling of a silicon anode under standard conditions [9], several others—Li_1Si_1 [10], $Li_{12}Si_7$ [11], Li_7Si_3 [12], $Li_{13}Si_4$ [13], β-$Li_{15}Si_4$ [14], $Li_{4.11}Si_1$ [15], $Li_{21}Si_5$ [16], $Li_{17}Si_4$ [17] and $Li_{22}Si_5$ [18]—have been synthesized at higher temperatures or pressures. Crystalline lithium-silicon compounds are characterized as Zintl-like phases based on their electronic structure [19, 20].

Diffusion coefficients are among the various physical quantities significantly affected by the presence of crystallographic defects in solids [21]. Such defects have different dimensionalities and can be intrinsic or extrinsic in nature. Intrinsic point defects include self-interstitials, vacancies, Schottky and Frenkel disorder, while extrinsic point defects are, for example, interstitial and isovalent or aliovalent substitutional foreign atoms. Computational research often focuses on point-defect-mediated diffusion mechanisms in solids, such as vacancy, interstitial, and interstitialcy mechanisms, because they typically require lower migration barriers than non-defect direct exchange, ring, and chain-like mechanisms [21]. As the knowledge gained from studying elementary migration mechanisms in crystalline compounds may be relevant to describing, for instance, amorphous systems within multiscale models, exploring lithium diffusivity in ordered Li silicides can be essential for enhancing the design of silicon anodes.

Experimentally, lithium diffusivity in amorphous Li_xSi has been measured using cyclic voltammetry, electrochemical impedance spectroscopy, and the galvanostatic intermittent titration technique [22], and the mechanisms of the electrochemically driven solid-state amorphization in Li–Si compounds [23] and of the phase transition from a-Li_xSi to c-$Li_{15}Si_4$ [24] have been investigated by microscopy and electron energy loss spectroscopy. Coulometric titration found Li diffusion coefficients around 6.0×10^{-5} cm^2 s^{-1} in crystalline $Li_{12}Si_7$, Li_7Si_3, $Li_{13}Si_4$, and $Li_{22}Si_5$ at 415 °C [25], while NMR studies have assigned distinct Li mobilities to specific crystallographic sites in $Li_{12}Si_7$ [26], as well as in Li_7Si_3, $Li_{13}Si_4$, and $Li_{15}Si_4$ [27]. Moreover, in $Li_{12}Si_7$, a one-dimensional Li diffusion process with an activation barrier of 0.18 eV was distinguished from two three-dimensional processes (0.32 eV and 0.55 eV) [28, 29].

Computationally, nudged elastic band (NEB) calculations have been used to analyze single lithium ion migration in both amorphous [30, 31] and crystalline Si, focusing on diffusion mechanism and energetics [32], electronic structure [33], the effect of strain [34], and comparing the Li–Si system with Na-Si [35], Li-Ge and Li-Sn [36]. Additionally, Li diffusion in amorphous Li_xSi [37, 38] and the process of mixing lithium with amorphous [39] or crystalline [39, 40] silicon have been studied by means of *ab initio* molecular dynamics (AIMD) simulations. Moreover, NEB calculations and AIMD simulations were performed to characterize Li diffusivity in the crystalline compounds Li_1Si_1 [41], $Li_{12}Si_7$ [42], and $Li_{13}Si_4$ [43]. Two studies examined all three Li_xSi_y, additionally including $Li_{15}Si_4$ [44, 45], and one study employed NEB migration barriers in kinetic Monte Carlo simulations of these four compounds [46].

All of these computational works dealing with lithium diffusion in Li_xSi_y have explored different point-defect-mediated diffusion mechanisms, but they often consider only a limited range of compounds or defects, or both. Another uncertainty concerns the selection of proposed diffusion pathways for NEB calculations, many of which are speculative and based on crystallographic principles, rather than obtained from AIMD simulations. In our recently published study [45], we sought to present a comprehensive picture of intrinsic point defects—specifically, Li vacancies, Li interstitials, and a Schottky defect—in four crystalline Li–Si compounds: Li_1Si_1, $Li_{12}Si_7$, $Li_{13}Si_4$ and $Li_{15}Si_4$. In this present work, we add extrinsic defects to the picture in the form of larger isovalent substitutional (Na, Ge) and interstitial (Na) atoms. While the effect of aliovalent P-doping on Li migration barriers has been studied in crystalline Si [23, 47], no extrinsic defects have yet been investigated in Li_xSi_y. Here, we explore meaningful lithium diffusion paths in the presence of Na and Ge atoms by combining AIMD simulations with NEB calculations.

2. Computational setup

2.1. Crystal structures

Figure 1 shows the crystal structures of all Li silicides studied here as supercells, as described in section 2.2. In the supporting information (figures S1–S4), the supercells contain interstitial sites and metastable positions, as detected in two previous works [44, 45]. Additionally, crystallographic Li sites are labeled. In this study, VESTA [48] and VMD [49] are used for crystal structure visualization. Table 1 provides relevant crystallographic data. Li_1Si_1, $Li_{12}Si_7$, $Li_{13}Si_4$, and $Li_{15}Si_4$ were considered here, since they are the reported crystalline Li–Si compounds without partially occupied Li sites for Li/Si ratios up to 3.75, the highest value observed during electrochemical lithiation.

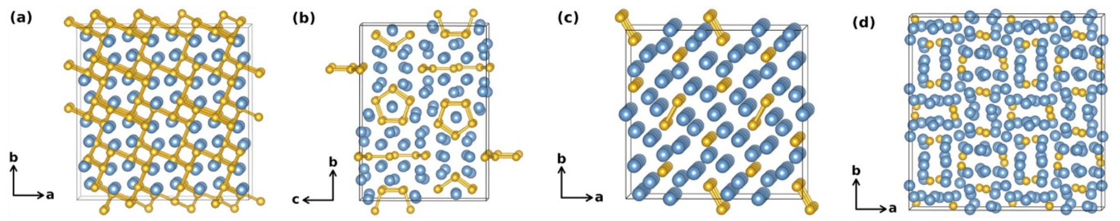

Figure 1. Crystal structures of (a) Li_1Si_1, (b) $Li_{12}Si_7$, (c) $Li_{13}Si_4$ and (d) $Li_{15}Si_4$ (Li: blue, Si: yellow). Reproduced from [45]. © The Author(s). Published by IOP Publishing Ltd. CC BY 4.0.

Table 1. Crystallographic data for lithium silicides included in this study. Reproduced from [45]. © The Author(s). Published by IOP Publishing Ltd. CC BY 4.0.

Compound	x/y	Space group	No. Li	No. Si	a (Å)	b (Å)	c (Å)	Reference
Li_1Si_1	1.00	88 ($I4_1/a$)	16	16	9.354	9.354	5.746	[10]
$Li_{12}Si_7$	1.71	62 ($Pnma$)	96	56	8.600	19.755	14.336	[11]
$Li_{13}Si_4$	3.25	55 ($Pbam$)	26	8	7.949	15.125	4.466	[13]
$Li_{15}Si_4$	3.75	220 ($I\bar{4}3d$)	60	16	10.687	10.687	10.687	[9]

Table 2. Summary of the investigated systems with extrinsic point defects.

Compound	Defect	System	Compound	Defect	System
Li_1Si_1	$\mathrm{Na}_{\mathrm{Li}}^{\mathrm{x}}$	Na @ Li1	$Li_{13}Si_4$	$\mathrm{Na}_{\mathrm{Li}}^{\mathrm{x}}$	Na @ Li1
	$\mathrm{Na}_{\mathrm{i}}^{\mathrm{x}}$	Na @ Int1			Na @ Li2
		Na @ Int2			Na @ Li7
	$\mathrm{Ge}_{\mathrm{Si}}^{\mathrm{x}}$	Ge @ Si1		$\mathrm{Na}_{\mathrm{i}}^{\mathrm{x}}$	Na @ Li2[a]
$Li_{12}Si_7$	$\mathrm{Na}_{\mathrm{Li}}^{\mathrm{x}}$	Na @ Li1			Na @ Li1/Li2[b]
		Na @ Li12			Na @ Int
	$\mathrm{Na}_{\mathrm{i}}^{\mathrm{x}}$	Na @ Int1		$\mathrm{Ge}_{\mathrm{Si}}^{\mathrm{x}}$	Ge @ Si2
		Na @ Int2	$Li_{15}Si_4$	$\mathrm{Na}_{\mathrm{Li}}^{\mathrm{x}}$	Na @ Li1
	$\mathrm{Ge}_{\mathrm{Si}}^{\mathrm{x}}$	Ge @ Si8			Na @ Li2
				$\mathrm{Na}_{\mathrm{i}}^{\mathrm{x}}$	Na @ Int
				$\mathrm{Ge}_{\mathrm{Si}}^{\mathrm{x}}$	Ge @ Si1

[a] One Na atom and one Li atom located at 1× Li2 (= split/dumbbell interstitial).

[b] One Na atom and four Li atoms located at 2× Li1 and 2× Li2 (= crowdion-like interstitial).

Li_1Si_1 [10] has a tetragonal structure with a single crystallographic site for Li and Si, respectively, while $Li_{15}Si_4$ [9] is cubic with two distinct Li sites and one Si site, making both compounds highly symmetric. In contrast, $Li_{12}Si_7$ [11], with 13 Li sites and 9 Si sites, and $Li_{13}Si_4$ [13], with 7 Li sites and 2 Si sites, are orthorhombic and exhibit lower overall symmetry. Various Si_n^{m-} polyanions are present in the Zintl-like Li_xSi_y phases [19, 20]. These Zintl ions include a network of threefold coordinated Si in Li_1Si_1 [10], planar Si_5 rings and Si_4 stars in $Li_{12}Si_7$ [11], Si_2 dumbbells and isolated Si in $Li_{13}Si_4$ [13], and solely isolated Si in $Li_{15}Si_4$ [9].

2.2. Investigated systems with point defects

All studied systems are presented in table 2, with additional details on their lattice constants provided in tables S1–S4 of the supporting information. The corresponding .xyz files are available as supplementary data. The systems were set up as supercells from their respective primitive cells according to: 2 × 2 × 2 for Li_1Si_1, 1 × 1 × 1 for $Li_{12}Si_7$, 2 × 1 × 3 for $Li_{13}Si_4$, and 2 × 2 × 1 for $Li_{15}Si_4$. Extrinsic point defects were then introduced into the resulting supercells as larger Na and Ge atoms. Isovalent Na and Ge were chosen so as not to alter the electronic structure by adding excess electrons or holes, but to isolate the effect of atomic size. For each Li–Si compound, systems containing either a Na interstitial ($\mathrm{Na}_{\mathrm{i}}^{\mathrm{x}}$) or a substitutional atom ($\mathrm{Na}_{\mathrm{Li}}^{\mathrm{x}}$ or $\mathrm{Ge}_{\mathrm{Si}}^{\mathrm{x}}$) were created. Interstitial sites and metastable positions were identified by combining visual inspection of *ab initio* MD trajectories from two previous studies [44, 45], geometrical analysis, and a method based on a repulsive pair potential [50]. The fractional coordinates of these sites are listed in table S5 of the supporting information. For each defect within each compound, the first system in table 2 serves as the starting structure for the AIMD simulation. Through diffusion within the simulated trajectory, the defect may migrate to a different lattice site.

2.3. Electronic structure and simulation methods

Density functional theory (DFT) [51, 52] calculations were carried out within the CP2K software package [53, 54]. The Kohn–Sham equations [52] are solved by the Quickstep (QS) module [54, 55] of CP2K using the Gaussian plane wave (GPW) method [56]. This method employs atom-centered Gaussians as a basis for the orbitals and plane waves as an auxiliary basis for the electronic density. For the calculations, the DZVP-MOLOPT-SR-GTH basis set [57] and GTH-PBE pseudopotentials [58–60] were applied. The plane-wave energy cutoff was set to 350 Ry, with a relative cutoff of 40 Ry. Given the large supercells, only the Γ point was sampled. Periodic boundary conditions were used in all calculations. The Perdew–Burke–Ernzerhof (PBE) functional [61, 62] was utilized for the exchange-correlation (XC) energy, with dispersion corrections included via the DFT-D3 method [63]. Although hybrid functionals are often adopted to improve the calculation of various physical properties [64, 65], methodological studies show that they are not guaranteed to outperform GGA functionals for metallic systems [66, 67]. Fermi–Dirac smearing [68] was applied at an electronic temperature of 600 K, and convergence of the self-consistent field (SCF) procedure was achieved using Broyden mixing [69] with a mixing parameter $\alpha = 0.2$. The SCF convergence criterion was set to 10^{-6}.

The lattice constants and atomic positions of the systems, whose preparation is discussed in section 2.2, needed to be relaxed prior to the AIMD simulations and NEB calculations. The Broyden–Fletcher–Goldfarb–Shanno (BFGS) minimizer [70–73] was employed to perform all geometry and cell optimizations in this study. At zero temperature and 1 atm pressure, the cell parameters and atomic coordinates of the supercells without defects, as well as those of all systems with defects, were initially fully relaxed. A correction factor, derived from the ratio of experimental (see table 1) to calculated lattice parameters of the systems without defects, was used to scale the calculated lattice parameters of the defect-containing systems. This approach corrects both the inaccuracies of the electronic structure method during cell optimization and the effects of thermal expansion. The cell parameters of the systems without defects were scaled in the same way to match the experimentally measured ones. Then, the atomic positions of all systems were fully re-optimized with the scaled lattice constants fixed, to create an initial configuration for AIMD simulations and NEB calculations.

For the calculation of defect formation energies and elastic constants, the atomic positions and lattice constants were again optimized for all systems, both with and without defects, at a higher level of theory. Modified DFT parameters included TZVP-MOLOPT-GTH (Si), TZVP-MOLOPT-SR-GTH (Li, Ge) and TZVPd-MOLOPT-SR-GTH-q9 (Na) basis sets, no dispersion correction, and a Monkhorst-Pack k-point sampling scheme [74] for Brillouin zone integration. The meshes are provided in supporting information, table S6. Equation (1) was used to obtain the defect formation energies [64],

$$E_{\text{form}}(\text{defect}) = E(\text{defect}) - E(\text{bulk}) - \sum_i n_i \mu_i. \tag{1}$$

The energies of the systems with and without defects are represented by E(defect) and E(bulk), respectively. The number of atoms of element i removed or added to convert the defect-free system into the defect-containing one is denoted by n_i, while μ_i corresponds to the chemical potential of a single atom. Here, μ_i is approximated by the energy of an atom in a fully relaxed supercell of the crystalline element i (Li, Si, Na, Ge). Applying a well-established stress–strain methodology from the literature [75], the elastic constants were calculated, as outlined in section S1.1 of the supporting information.

AIMD simulations were carried out in a canonical ensemble (NVT) at 500 K for $Li_{12}Si_7$ and $Li_{13}Si_4$, and at 800 K for Li_1Si_1 and $Li_{15}Si_4$. Temperature control was provided by a Nosé-Hoover chain thermostat [76, 77], and a time step of 1 fs was chosen. Equilibration was performed using massive thermostatting with a time constant of $\tau = 10$ fs for 1 ps. After an additional 1 ps with $\tau = 100$ fs, a 100 ps trajectory was generated for analysis using global thermostatting with $\tau = 100$ fs. The mean square displacements (MSDs) were used to calculate the diffusion coefficients; for further details, refer to section S1.2 in the supporting information.

Climbing image [78] NEB [79–82] (CI-NEB) calculations were performed on the atomistic migration paths obtained from the AIMD simulations. Including fully relaxed initial and final atomic configurations, that were fixed for the NEB calculation, 16 replicas were used to map each path.

Table 3. AIMD simulation results for Li diffusion coefficients D_{Li} / (10^{-3} Å^2 ps^{-1} = 10^{-7} cm^2 s^{-1}) in crystalline lithium silicides with extrinsic defects: 500 K data for $Li_{12}Si_7$ and $Li_{13}Si_4$, 800 K data for Li_1Si_1 and $Li_{15}Si_4$, values for systems without non-stoichiometric defects taken from [44].

Compound	Stoichiometric [44]	Na_{Li}^{x}	Na_{i}^{x}	Ge_{Si}^{x}
Li_1Si_1	0.0	0.0	0.5	0.0
$Li_{12}Si_7$	11.6	13.1	12.3	18.4
$Li_{13}Si_4$	39.5	17.6	34.1	93.4
$Li_{15}Si_4$	0.2	0.0	15.9	0.0

3. Results and discussion

3.1. Substitutional Na atoms

AIMD simulations were performed to determine Li diffusivities in Li_xSi_y in the presence of extrinsic point defects (see section 2.2 for details of the simulation cells). Simulations were carried out at 500 K for $Li_{12}Si_7$ and $Li_{13}Si_4$, and at 800 K for Li_1Si_1 and $Li_{15}Si_4$, since previous results showed that 500 K is insufficient to observe diffusion in the latter two compounds [44, 45]. These temperatures were chosen to match those used in our earlier studies, allowing direct comparison [44, 45]. Figures S5–S7 in the supporting information show representative plots of temperature and the conserved quantity versus simulation time, demonstrating the stability of the systems.

Using equation S5, the diffusion coefficients D_{Li} were calculated from the Li MSDs (see supporting information, figure S8) and are compiled in table 3. For comparison, the values for systems without non-stoichiometric defects were taken from [44]. Those results were discussed alongside previously experimentally measured values in two recent studies [44, 45]. In conclusion, stoichiometric systems of $Li_{12}Si_7$ and $Li_{13}Si_4$ exhibit higher Li ion conductivities than Li_1Si_1 and $Li_{15}Si_4$. This arises from low-energy diffusion pathways due to Frenkel disorder in $Li_{12}Si_7$ and due to a transition to a metastable structure in $Li_{13}Si_4$.

Li diffusion coefficients for the four compounds with a substitutional Na atom are reported in table 3. Zero diffusion is observed in Li_1Si_1 and $Li_{15}Si_4$, whereas $Li_{12}Si_7$ and $Li_{13}Si_4$ exhibit fast ionic conduction. Overall, Li diffusivities remain similar to those in stoichiometric systems, with the only significant decrease—halving—occuring in $Li_{13}Si_4$. For comparison, D_{Li} for in-plane diffusion in the common anode material graphite is 4.4×10^{-6} cm^2 s^{-1} [83], and 10^{-6} to 10^{-5} cm^2 s^{-1} for diffusion in the superionic conductor $Li_{10}GeP_2S_{12}$ (LGPS) [84]. Thus, the Li diffusivities in $Li_{12}Si_7$ and $Li_{13}Si_4$ are comparable to these fast ionic conductors. The Na diffusion coefficient D_{Na} is 0.0 in Li_1Si_1 and $Li_{15}Si_4$, 15.4 in $Li_{12}Si_7$, and 10.7 in $Li_{13}Si_4$, all values in 10^{-3} Å^2 ps^{-1}. Thus, Na atoms diffuse on a scale comparable to Li. Spatially resolved D_{Li}, which characterize diffusion (an)isotropy, are provided in table S7 of the supporting information. Diffusion remains anisotropic in $Li_{12}Si_7$ and quasi one-dimensional in $Li_{13}Si_4$, showing no fundamental differences from the stoichiometric systems. Only one observed diffusion step in $Li_{13}Si_4$ has components in both the y and z directions, see table S15 in the supporting information.

The contribution of individual crystallographic sites to overall ion mobility can be quantified using the protocol detailed in [44]. For each Li_xSi_y compound, the lattice is represented by the relaxed atomic positions of the stoichiometric system, including metastable positions and interstitial sites. Red lines connect pairs of lattice sites where atomic jumps are observed in the MD trajectory, and the line thickness reflects the jump count on a logarithmic scale. Figure 2 illustrates this analysis for $Li_{13}Si_4$, while the corresponding results for Li_1Si_1, $Li_{12}Si_7$ and $Li_{15}Si_4$ can be found in figures S9–S11 of the supporting information.

In two previous studies, the mobility of distinct Li sites was thoroughly explored in stoichiometric systems [44] and in systems with intrinsic defects [45]. Stoichiometric Li_1Si_1 and $Li_{15}Si_4$ exhibit only immobile sites on the AIMD timescale, whereas $Li_{12}Si_7$ and $Li_{13}Si_4$ have sites with mobilities ranging from immobile to highly mobile. Upon introduction of intrinsic defects, more Li sites become mobile in all four Li_xSi_y, and the degree of mobility depends on the particular site and compound. Here, we focus solely on outlining the changes caused by extrinsic defects. In systems with a substitutional Na atom, no jumps were detected in Li_1Si_1 and $Li_{15}Si_4$, consistent with the D_{Li} values discussed above. $Li_{12}Si_7$ exhibits many jumps reflecting anisotropic diffusion similar to that of the stoichiometric system, with certain new (Li5-Li12, Li7-Li8, Li7-Li11, Li7-Li12, Li11-Li13) and missing (Li1-Int1, Li8-Li9) connections, that could indicate energetic effects of the Na atom on other diffusion paths. Note that the most frequent Na position in the AIMD trajectories is colored green in the figures. In $Li_{13}Si_4$, many jumps follow the known highly anisotropic pattern, matching the stoichiometric system except for a few detection errors.

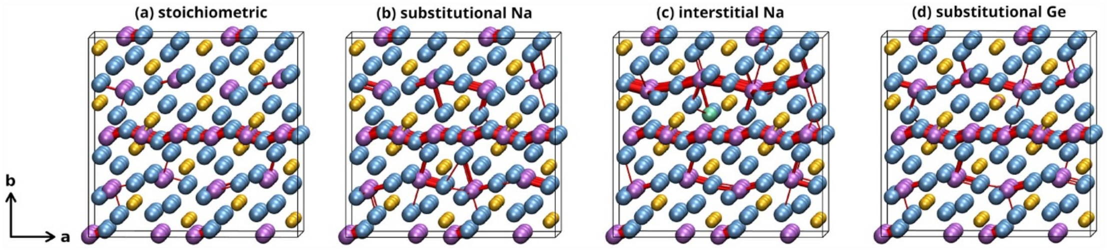

Figure 2. Atomic jumps between pairs of lattice sites (red lines) in AIMD simulations of $Li_{13}Si_4$ systems with (a) no non-stoichiometric defect [44], Reproduced from [45]. © The Author(s). Published by IOP Publishing Ltd. CC BY 4.0. (b) A substitutional Na atom, (c) an interstitial Na atom, and (d) a substitutional Ge atom. Li sites are shown in blue, Si sites in yellow, metastable or interstitial sites in violet, the most frequent site of Na in green, and the Ge site in pink.

Sections 2.1 and 2.2 provide details on the Li_xSi_y crystal structures, including the crystallographic Li and Si sites as well as metastable positions and interstitial sites. For the AIMD simulations, initial configurations were generated by substituting Na for Li at a Li1 site in all four compounds. Subsequently, Na did not migrate in Li_1Si_1 and $Li_{15}Si_4$. In $Li_{12}Si_7$, Na moved to an adjacent Int1 site in the initial geometry optimization, thereby creating a Li1 vacancy, and then migrated between Int1 and Li12 in the MD trajectory. In the $Li_{13}Si_4$ trajectory, Na hopped between Li1, Li2 and M2 sites before becoming immobilized on Li7.

To achieve a comprehensive atomistic picture of cation mobility, diffusion paths for both Li and Na—extracted from the AIMD trajectories or proposed on theoretical grounds—were further investigated using NEB calculations. The migration mechanisms and resulting energy barriers are summarized in tables S11 and S15 of the supporting information, and the fully relaxed paths with their energy profiles are provided as supplementary data (.xyz and .txt files, respectively). Path names are consistent with [45] for direct comparability. For clarity, paths within each compound are numbered sequentially, and corresponding paths in different systems share the same number. In non-stoichiometric systems, a suffix '_def' denotes defect migration, '_near' indicates that at least one migrating atom is within 3 Å of the defect, and '_far' marks paths occurring more than 3 Å from the defect.

Migration of substitutional Na atoms follows pathways previously identified for Li atoms showing various diffusion mechanisms [44, 45], with energy barriers ranging from 0.04 eV to 0.26 eV in $Li_{12}Si_7$ and from 0.00 eV to 0.72 eV in $Li_{13}Si_4$. In $Li_{12}Si_7$, this includes Frenkel-pair formation and subsequent vacancy jumps with migration energies of 0.13 eV and 0.04 eV (path (39)_def), followed by an interstitialcy pathway $Na_{Int1} \rightarrow Li12 \rightarrow Li12 \rightarrow Int1$ with barriers of 0.20 eV and 0.26 eV (path (27)_def). In $Li_{13}Si_4$, Na migrates via the same collective, chain-like motion reported in [43–45], here represented by paths (44)_I_def_a and (44)_I_def_b, exhibiting low barriers of 0.00 eV to 0.09 eV. Path (58)_def shows a five-ring mechanism with higher barriers of 0.72 eV and 0.69 eV typical of non-defect collective diffusion, ultimately immobilizing Na on Li7. A detailed comparison of Na versus Li migration energetics is given in section 3.2, along with systems with interstitial Na atoms, where interstitial Na relaxes onto a regular lattice site, creating a Li interstitial and effectively becoming substitutional Na. Li migration barriers in representative fast-ion conductors range from 0.28 to 0.30 eV for in-plane diffusion in graphite [83] and from 0.17 to 0.28 eV for $Li_{10}GeP_2S_{12}$ [84]. These values are comparable to those computed for several paths in $Li_{12}Si_7$ and $Li_{13}Si_4$.

The bulk and shear moduli of all crystalline Li–silicide systems were derived from their elastic constants, which were determined following the procedure in section S1.1, and are listed in table 4. As the Li/Si ratio increases and the Si-Si connectivity diminishes, both moduli decrease, indicating progressive softening. In particular, the Si-Si bonding network renders Li_1Si_1 notably stiffer than $Li_{12}Si_7$, $Li_{13}Si_4$ and $Li_{15}Si_4$. The bulk modulus of polycrystalline graphite is 7.3 to 10.7 GPa [85], and that of $Li_{10}GeP_2S_{12}$ is 27.3 GPa [86], making the crystalline Li–Si compounds less compressible than soft graphite, but rather moderately stiff compared with typical solids. Although there is no simple correlation between the elastic moduli and the Li diffusivity D_{Li} across different compounds, defect-induced changes in lattice stiffness can alter migration barriers within a compound, as discussed for intrinsic defects in Li_xSi_y in [45] (see also the cBΩ model [87]). Substituting a Na atom into the lattice lowers the bulk moduli K_V by

Table 4. Voigt-averaged bulk moduli (K_V, in GPa) and shear moduli (G_V, in GPa) of Li_xSi_y systems, including both stoichiometric compositions [45] and those with extrinsic defects.

compound	system	K_V	G_V	compound	system	K_V	G_V
			stoichiometric [45]				
Li_1Si_1		52.9	38.9	$Li_{13}Si_4$		32.7	29.3
$Li_{12}Si_7$		37.4	33.9	$Li_{15}Si_4$		30.2	23.1
			Na^x_{Li}				
Li_1Si_1	Na @ Li1	52.5	38.5	$Li_{13}Si_4$	Na @ Li1	35.3	30.6
$Li_{12}Si_7$	Na @ Li1	36.5	33.1		Na @ Li2	32.6	29.2
	Na @ Li12	36.0	33.3		Na @ Li7	30.4	29.6
				$Li_{15}Si_4$	Na @ Li1	29.6	22.9
					Na @ Li2	29.1	22.7
			Na^x_i				
Li_1Si_1	Na @ Int1	52.8	37.7	$Li_{13}Si_4$	Na @ Li2[a]	32.7	28.6
	Na @ Int2	52.3	38.0		Na @ Li1/Li2[b]	33.6	28.2
$Li_{12}Si_7$	Na @ Int1	35.6	33.2		Na @ Int	32.9	31.9
	Na @ Int2	36.7	32.5	$Li_{15}Si_4$	Na @ Int	29.4	22.8
			Ge^x_{Si}				
Li_1Si_1	Ge @ Si1	52.7	38.6	$Li_{13}Si_4$	Ge @ Si2	32.6	29.4
$Li_{12}Si_7$	Ge @ Si8	37.0	33.6	$Li_{15}Si_4$	Ge @ Si1	30.2	23.1

[a] One Na atom and one Li atom located at 1× Li2 (= split/dumbbell interstitial).

[b] One Na atom and four Li atoms located at 2× Li1 and 2× Li2 (= crowdion-like interstitial).

Table 5. Energies of extrinsic defect formation (E_{form}, in eV) in Li_xSi_y systems.

Compound	System	E_{form}	Compound	System	E_{form}
			Na^x_{Li}		
Li_1Si_1	Na @ Li1	0.60	$Li_{13}Si_4$	Na @ Li1	1.07
$Li_{12}Si_7$	Na @ Li1	0.54		Na @ Li2	0.72
	Na @ Li12	0.34		Na @ Li7	1.14
			$Li_{15}Si_4$	Na @ Li1	0.53
				Na @ Li2	0.61
			Na^x_i		
Li_1Si_1	Na @ Int1	2.23	$Li_{13}Si_4$	Na @ Li2[a]	1.08
	Na @ Int2	1.30		Na @ Li1/Li2[b]	1.33
$Li_{12}Si_7$	Na @ Int1	0.25		Na @ Int	0.59
	Na @ Int2	0.32	$Li_{15}Si_4$	Na @ Int	0.67
			Ge^x_{Si}		
Li_1Si_1	Ge @ Si1	−0.14	$Li_{13}Si_4$	Ge @ Si2	−0.45
$Li_{12}Si_7$	Ge @ Si8	−0.37	$Li_{15}Si_4$	Ge @ Si1	−0.47

[a] One Na atom and one Li atom located at 1× Li2 (= split/dumbbell interstitial).

[b] One Na atom and four Li atoms located at 2× Li1 and 2× Li2 (= crowdion-like interstitial).

-0.4 … -1.4 GPa and the shear moduli G_V by -0.2 … -0.8 GPa, compared to defect-free Li_1Si_1, $Li_{12}Si_7$ and $Li_{15}Si_4$, indicating softening. In $Li_{13}Si_4$, the effect depends on the lattice site: ΔK_V ranges from $+2.6$ to -2.3 GPa and ΔG_V from $+1.3$ to -0.1 GPa, reflecting either stiffening or softening.

In addition to defect migration energies, quantifying defect concentrations via their formation energies is essential for evaluating their impact on diffusion. These energies were calculated for all extrinsic defects as described in section 2.3 and are presented in table 5. For substitutional Na atoms, the values are moderate and range from 0.3 to 0.5 eV in $Li_{12}Si_7$, 0.5 to 0.6 eV in $Li_{15}Si_4$, 0.6 eV in Li_1Si_1, and 0.7 to 1.1 eV in $Li_{13}Si_4$.

Overall, substitutional Na atoms do not significantly alter diffusion in the compounds studied. Li diffusion coefficients and anisotropies remain essentially unchanged from the stoichiometric systems, and Na diffusivities are of the same order as D_{Li}. Consequently, no diffusion is observed in Li_1Si_1 and $Li_{15}Si_4$, whereas low-energy migration paths in $Li_{12}Si_7$ and $Li_{13}Si_4$ enable fast diffusion. Moreover, on most lattice sites, substitutional Na atoms soften the lattice, and their moderate formation energies imply that they can form in non-negligible concentrations at equilibrium with a Na reservoir.

3.2. Interstitial Na atoms

Li diffusivities in Li_xSi_y systems initially containing a Na interstitial are reported in table 3. The AIMD simulations show that a Na interstitial is unstable in all four compounds: within the first few picoseconds, Na substitutes a Li atom, creating a Li interstitial and a substitutional Na atom. Hence, the observed diffusivities can be viewed as those of a Li interstitial combined with a substitutional Na atom, see [45] and section 3.1. Values of D_{Li} are consistent with those of systems with only Li interstitials: high in $Li_{12}Si_7$, $Li_{13}Si_4$ and $Li_{15}Si_4$, and lower, but non-zero, in Li_1Si_1. Thus, Li interstitials promote diffusion in Li_1Si_1 and $Li_{15}Si_4$, but have no significant impact on diffusivity in $Li_{12}Si_7$ and $Li_{13}Si_4$, whether compared to the stoichiometric systems or to those containing only substitutional Na atoms. The Na diffusivity D_{Na} / 10^{-3} Å^2 ps^{-1} is 0.1 in Li_1Si_1 and $Li_{12}Si_7$, 0.5 in $Li_{13}Si_4$, and 0.0 in $Li_{15}Si_4$, confirming immediate Na immobilisation on a regular lattice site. This occurs even more rapidly than for substitutional Na defects (see section 3.1), implying a dependence on the initial Na site. Values of D_x, D_y and D_z are given in table S7 of the supporting information. Li_1Si_1 diffusivity is too low for anisotropy analysis. The (an)isotropies again match those for Li interstitials discussed in [45]: diffusion is isotropic in $Li_{15}Si_4$, and anisotropic in $Li_{12}Si_7$ and $Li_{13}Si_4$, with $Li_{12}Si_7$ showing altered $D_x/D_y/D_z$ ratios and $Li_{13}Si_4$ exhibiting a new low D_y and medium D_z, compared to the stoichiometric systems.

Jumps between lattice sites are shown in figures 2(c) and S6–S8. As discussed for Li interstitials in [45] and consistent with D_{Li}, no jumps were detected in Li_1Si_1, whereas numerous jumps occur in $Li_{12}Si_7$, $Li_{13}Si_4$ and $Li_{15}Si_4$. In $Li_{12}Si_7$, notable missing connections—Na_{Li12}-Int, Li1-Int (around Na_{Li12}), Li8-Li9, Li8-M1, Li9-M2 and Li9-Li10 - suggest that Na hinders certain migration paths. In $Li_{13}Si_4$, diffusion is strongly anisotropic: the Li1-M1, Li1-M2, Li2-M2 and Li6-Int connections along the x-direction are highly populated, while Li3-Int jumps in the z-direction occur moderately frequently. In $Li_{15}Si_4$, the Li1-Li1, Li1-Li2, Li1-Int, Li2-Int and Int-Int connections cause isotropic diffusion.

Relevant interstitial sites in the Li_xSi_y compounds were identified as described in sections 2.1 and 2.2. All four Li silicides have either one ($Li_{13}Si_4$, $Li_{15}Si_4$) or two (Li_1Si_1, $Li_{12}Si_7$) regular interstitial sites; additionally, split interstitials and crowdion-like interstitials can form in the cation sublattice of $Li_{13}Si_4$. For the AIMD simulations, Na interstitials were initially placed on Int1 in Li_1Si_1 and $Li_{12}Si_7$, on Li2 (as a split interstitial) in $Li_{13}Si_4$, and on Int in $Li_{15}Si_4$. Within the first few picoseconds −1.5 ps in Li_1Si_1, 2 ps in $Li_{12}Si_7$, 4 ps in $Li_{13}Si_4$, and 2 ps in $Li_{15}Si_4$—each Na interstitial substituted a lattice Li, forming a Li interstitial on Int2, Int1, Int, and Int, and a substitutional Na atom on Li1, Li12, Li7, and Li1, respectively. Again, observed as well as theoretically constructed diffusion pathways were studied via NEB calculations; the corresponding results are compiled in tables S9, S12, S16 and S19 of the supporting information and provided as supplementary data.

As observed for Li interstitials [45], Na interstitials also migrate via interstitialcy mechanisms. The migration barriers for these paths are 0.30 and 1.29 eV in Li_1Si_1, 0.00 and 0.04 eV in $Li_{12}Si_7$, 0.00 and 0.42 eV in $Li_{13}Si_4$, and 0.03–0.58 eV in $Li_{15}Si_4$. Na interstitialcy paths involve two atoms in Li_1Si_1, $Li_{12}Si_7$ and $Li_{13}Si_4$, and three atoms in $Li_{15}Si_4$. Direct interstitial Na hopping was also investigated in Li_1Si_1 and $Li_{15}Si_4$, finding minimum barriers of 0.23 eV and 0.00 eV, respectively, making this mechanism, in principle, possible in both compounds. However, the low dynamic stability of Na interstitials indicates that additional barriers exist to populate these interstitials, making the low Na migration barriers observed here rather irrelevant in practice. Discussing observed interstitialcy paths in more detail, in Li_1Si_1 path (3)_def_b corresponds to relaxation of Na_{Int1} onto Li1 and formation of Li_{Int2}, with barriers of 0.30 eV and 1.29 eV. In $Li_{12}Si_7$, path (40)_def is the substitution of Li12 by Na_{Int1} and creation of Li_{Int1}, showing very low barriers of 0.04 eV and 0.00 eV. In $Li_{13}Si_4$, path (48)_def involves Na from a split interstitial on Li2 pushing an adjacent Li7 onto an interstitial site Int, with barriers of 0.00 eV and 0.42 eV. Finally, in $Li_{15}Si_4$ several paths follow the pattern $Na_{\mathrm{Int}} \rightarrow \mathrm{Li1} \rightarrow \mathrm{Li1} \rightarrow \mathrm{Int}$, see (62)_def to (64)_def; among these, path (62)_def has the lowest barriers of 0.16 eV and 0.03 eV.

We now want to compare Na and Li migration energies from NEB calculations for Li_xSi_y systems with extrinsic defects against those of the corresponding pathways in systems without extrinsic defects, to quantify their impact on diffusion energetics. Migration barriers in systems with substitutional and interstitial Na atoms are analyzed together here, since interstitial Na diffusion typically yields substitutional Na atoms, as described above. Individual data for the systems discussed in section 3.1 and in this section can be found in figures S12 and S13 of the supporting information, and the combined results are shown in figure 3.

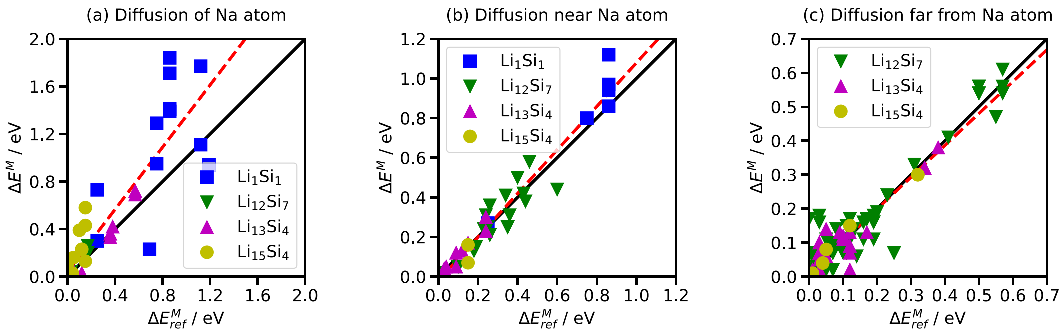

Figure 3. Energy barriers for migration ΔE^M: (a) Na atom diffusion, (b) Li diffusion near a Na atom (< 3 Å), and (c) Li diffusion farther from a Na atom (> 3 Å), correlated with migration barriers $\Delta E^M_{\mathrm{ref}}$ in systems without extrinsic defects. Black lines represent identity lines, red dashed lines show linear fits of the form $y = mx + n$, with (a) $m = 1.31$, $n = 0.04$, (b) $m = 1.10$, $n = -0.02$, and (c) $m = 0.94$, $n = 0.01$.

In figure 3(a), the migration energies of substitutional and interstitial Na atoms are compared with those of Li atoms in corresponding paths. On average, Na migration barriers are 31% higher, with most data points at or above the identity line and showing substantial scatter. This can be interpreted as a consequence of additional lattice strain during migration from Na's larger atomic radius. Figure 3(b) compares Li migration near a Na atom against Li diffusion near Li. For $\mathrm{Li_{12}Si_7}$, $\mathrm{Li_{13}Si_4}$, and $\mathrm{Li_{15}Si_4}$, the points cluster around the identity line; for $\mathrm{Li_1Si_1}$, they lie above it. With up to 0.3 eV of spread, barriers increase on average by 10%, again reflecting local strain due to Na's larger size. Figure 3(c) shows Li migration barriers at distances > 3 Å from a Na atom. Here, Na substitution lowers barriers by only 6% on average, with data scattered within ± 0.2 eV of the identity line, showing that paths can either increase or decrease in energy and underscoring the minor magnitude of this effect.

The bulk and shear moduli of crystalline $\mathrm{Li}_x\mathrm{Si}_y$ with a Na interstitial are shown in table 4. Compared with the corresponding systems containing a Li interstitial [45], bulk moduli K_V decrease by 0.0 … -0.8 GPa and shear moduli G_V by -0.2 … -1.0 GPa in $\mathrm{Li_1Si_1}$, $\mathrm{Li_{12}Si_7}$ and $\mathrm{Li_{15}Si_4}$. In $\mathrm{Li_{13}Si_4}$, the effect depends on the interstitial position: K_V increases by $+1.0$ … $+0.3$ GPa, while G_V varies between $+2.5$ … -1.3 GPa. Thus, Na interstitials soften the lattice even more than Li interstitials in $\mathrm{Li_1Si_1}$, $\mathrm{Li_{12}Si_7}$ and $\mathrm{Li_{15}Si_4}$, whereas in $\mathrm{Li_{13}Si_4}$ they increase K_V but have an ambiguous lattice effect on G_V. The magnitude of softening in the first three compounds is comparable to that caused by a substitutional defect $\mathrm{Na^x_{Li}}$, see section 3.1, which possibly contributes to the modest average barrier reductions discussed for figure 3(c).

Interstitial Na formation energies are given in table 5. They range from approximately 0.3 eV in $\mathrm{Li_{12}Si_7}$, to 0.6–1.3 eV in $\mathrm{Li_{13}Si_4}$, 0.7 eV in $\mathrm{Li_{15}Si_4}$, and 1.3–2.2 eV $\mathrm{Li_1Si_1}$. To examine the effect of spin polarization on the energetics of $\mathrm{Li}_x\mathrm{Si}_y$ systems containing Na interstitials, E_{form} were recalculated using spin-polarized calculations. The resulting values differ by less than ± 0.05 eV from those obtained without spin polarization, indicating that the effect is negligible in the studied systems. Compared with the sum of the lowest formation energies for a Li interstitial [45] and a substitutional Na atom, the lowest Na interstitial formation energy is higher by 0.45 eV in $\mathrm{Li_1Si_1}$, 0.12 eV in $\mathrm{Li_{12}Si_7}$, and 0.16 eV in $\mathrm{Li_{13}Si_4}$, but 0.08 eV lower in $\mathrm{Li_{15}Si_4}$. Thus, in $\mathrm{Li_1Si_1}$, $\mathrm{Li_{12}Si_7}$, and $\mathrm{Li_{13}Si_4}$, the combined $\mathrm{Na^x_{Li}} + \mathrm{Li^x_i}$ configuration is energetically favored over $\mathrm{Na^x_i}$, whereas the reverse is true in $\mathrm{Li_{15}Si_4}$. Although this thermodynamic driving force explains the initial $\mathrm{Li^x_{Li}} + \mathrm{Na^x_i} \rightarrow \mathrm{Na^x_{Li}} + \mathrm{Li^x_i}$ process in $\mathrm{Li_1Si_1}$, $\mathrm{Li_{12}Si_7}$, and $\mathrm{Li_{13}Si_4}$, the same process occurs almost immediately in the AIMD simulation of $\mathrm{Li_{15}Si_4}$. This discrepancy may reflect different effects, such as different levels of theory, entropic contributions, or energetic interactions between $\mathrm{Na^x_{Li}}$ and $\mathrm{Li^x_i}$. Overall, it can be concluded that Na interstitials are not stable in $\mathrm{Li}_x\mathrm{Si}_y$, but instead form Li interstitials and substitutional Na atoms.

In summary, Na interstitials relax almost instantaneously—via two- or three-atom interstitialcy paths—into substitutional Na atoms and Li interstitials. This Na immobilisation has near-zero migration barriers in $\mathrm{Li_{12}Si_7}$, $\mathrm{Li_{13}Si_4}$, and $\mathrm{Li_{15}Si_4}$, and a low-to-moderate barrier in $\mathrm{Li_1Si_1}$; however, the energy profiles are considerably asymmetric. Consequently, diffusivities and (an)isotropies are governed solely by Li interstitials. On average, Na migration barriers are 31% higher than the corresponding Li-only paths, and Li migration in the vicinity of Na atoms exhibits 10% higher barriers, both increases likely due to Na's larger atomic radius; by contrast, lattice softening possibly reduces migration barriers far from Na by 6% on average.

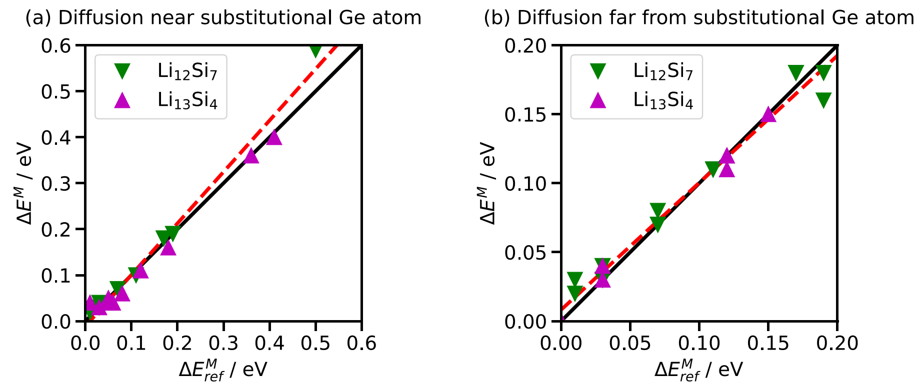

Figure 4. Energy barriers for migration ΔE^M: (a) Li diffusion near a substitutional Ge atom (< 3 Å), and (b) Li diffusion farther from a substitutional Ge atom (> 3 Å), correlated with migration barriers $\Delta E^M_{\mathrm{ref}}$ in stoichiometric systems. Black lines represent identity lines, red dashed lines show linear fits of the form $y = mx + n$, with (a) $m = 1.12$, $n = -0.01$, and (b) $m = 0.92$, $n = 0.01$.

3.3. Substitutional Ge atoms

The Li diffusion coefficients for compounds containing one substitutional Ge atom are listed in table 3. $Li_{12}Si_7$ and $Li_{13}Si_4$ remain good ionic conductors, whereas no diffusion was detected in Li_1Si_1 and $Li_{15}Si_4$. Overall, D_{Li} is of the same order of magnitude in stoichiometric systems and those with substitutional Na or Ge atoms, but it reaches its highest values in Ge-substituted $Li_{12}Si_7$ and $Li_{13}Si_4$. Note that the Ge atoms themselves do not migrate. Spatially resolved Li diffusivities are provided in table S7 of the supporting information. In $Li_{12}Si_7$, the diffusion anisotropy closely matches that of the stoichiometric system. In $Li_{13}Si_4$, Li diffusion is quasi one-dimensional, with only minor y- and z-components, similar to the results observed in the Na-substituted system. For the Ge-substituted system, the diffusion paths causing these components are unaffected in energy by the presence of Ge, see figure 4 and table S17. Consequently, they should, in principle, also occur in the stoichiometric system with the same probability; their apparent absence there is most likely due to the limited time scale of the AIMD simulations. Examples include the Frenkel-disorder paths (46) and (47).

Jumps between lattice sites are illustrated in figures 2(d) and S6–S8, with Ge atoms colored pink. In Li_1Si_1 and $Li_{15}Si_4$, no jumps—apart from artifacts—were detected. In $Li_{12}Si_7$, both the number and the anisotropy of jumps closely match those of the stoichiometric system. Unlike in the Na-substituted compound, no connections are missing in the Ge-substituted system. A few new, thin connections appear, though they contribute negligibly to the overall diffusivity. In $Li_{13}Si_4$, the jump pattern associated with path (44) is observed again (Li1-M1, Li1-M2, Li2-M2), accounting for a large fraction of D_x. Because a Frenkel defect forms in this AIMD trajectory, unlike in the stoichiometric system, connections known from the systems with Li interstitials [45] are also observed, as shown in figure 2(c). Specifically, these are the Li3-Int jumps along z-direction and the Li6-Int jumps along x-direction from paths (49) and (50), respectively. The component D_y arises mainly from Frenkel defect formation paths (46) and (47). Overall, a quasi 1D jump pattern along x-direction is obtained, as discussed above.

Ge atoms substitute Si atoms at lattice sites Si1, Si8, Si2 and Si1 in Li_1Si_1, $Li_{12}Si_7$, $Li_{13}Si_4$ and $Li_{15}Si_4$, respectively. As with Si atoms, Ge atoms do not diffuse in the AIMD simulations. The results of NEB calculations on the observed Li migration paths are given as supplementary data and in tables S13 and S17 of the supporting information. The obtained migration energy barriers are further illustrated, relative to those in stoichiometric systems, in figure 4.

Figures 4(a) and (b) show the changes in migration barriers at distances within 3 Å of a substitutional Ge atom and beyond 3 Å, respectively. On average, the barriers increase by 12% in the former case and decrease by 8% in the latter, yet all data points lie tightly distributed around the identity line. Although these trends could be attributed to the larger atomic radius of Ge and lattice softening, the effects are quite minor, comparable in magnitude to those observed for Na, but exhibiting a smaller spread, see figure 3. Note also that the limited number of compounds and data points reduces the significance of these observations.

Elastic moduli for systems containing substitutional Ge atoms can be found in table 4. Relative to the stoichiometric systems, the bulk moduli K_V change by $\pm 0.0 \ldots -0.4$ GPa and the shear moduli G_V by $+0.1 \ldots -0.3$ GPa, indicating at most a very slight lattice softening, that is consistent with the small effect on migration energies discussed above. This softening is less pronounced than that caused by

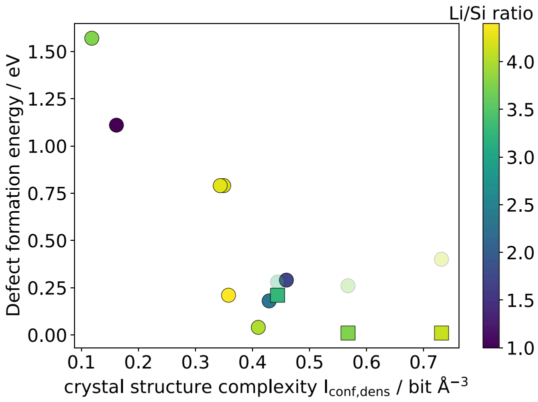

Figure 5. Lowest formation energies (in eV) of Frenkel defects (circles) and metastable structures (squares) in crystalline Li_xSi_y, plotted against volume-normalized configurational crystal structure complexity (in bits/Å^3). Color coding indicates Li/Si ratio from low (blue) to high (yellow). For compounds in which a metastable structure can form additionally to a Frenkel defect, solid symbols denote the lower-energy structure, while transparent symbols denote the higher-energy one.

substitutional Na atoms. The formation energies for substitutional Ge are given in table 5 and range from −0.1 eV to −0.5 eV, implying essentially zero energetic cost for Ge substitution. Therefore, Ge incorporation into the lattice is significantly more favorable than Na incorporation.

In summary, substituting Ge into the Si sublattice of Li_xSi_y has a negligible effect on Li diffusivity, diffusion anisotropy, and migration energy barriers near and far from the Ge atom. This finding is consistent with the very slight lattice softening and the energetically favorable formation of Ge defects, which likely stems from the almost negligible local lattice strain. Of the compounds considered, Li_1Si_1 and $Li_{15}Si_4$ show no diffusion, whereas $Li_{12}Si_7$ and $Li_{13}Si_4$ exhibit high Li diffusivities.

3.4. Li diffusion and crystal structure complexity

In the present work, as well as in two previous studies [44, 45], Li diffusion in crystalline Li_xSi_y was investigated systematically. Nevertheless, no fundamental atomistic explanation for the vastly different Li diffusivities among these compounds has been identified. In the following analysis, we include an extended set of compounds from the Li–Si phase diagram to help establish such an explanation. In addition to those already discussed in this work (Li_1Si_1, $Li_{12}Si_7$, $Li_{13}Si_4$, $Li_{15}Si_4$), we consider the most stable superstructure of Li_7Si_3 as discussed in [88], β-$Li_{15}Si_4$ [14], models A (Li_4Si) and B ($Li_{4.125}Si$) of $Li_{4.11}Si$ as proposed in [15], $Li_{21}Si_5$ [16], $Li_{17}Si_4$ [17], and $Li_{22}Si_5$ [18].

Since Li diffusion has been shown to be mediated by intrinsic defects and the variation in defect formation energies exceeds that of migration energies—making E_{form} more decisive than ΔE^M [44, 45]—we now focus on Frenkel defect formation to assess Li diffusivity in stoichiometric Li_xSi_y systems. As described in section 2.3, we computed the formation energies E_{form} of all possible Li vacancies and interstitials to identify the lowest Frenkel defect formation energy in each compound. Additionally, in $Li_{13}Si_4$, β-$Li_{15}Si_4$, and model B of $Li_{4.11}Si$, a metastable structure can form by concertedly shifting a row of Li atoms by half the Li-Li distance. The transition to these metastable structures also provides a pathway for Li diffusion. Accordingly, their formation energies are also evaluated, each of which is lower than the lowest Frenkel defect formation energy in the respective compound. All obtained values are presented in table S20 of the supporting information.

The lowest E_{form} of a Frenkel defect or metastable structure is a measure of the number of defects mediating Li diffusion in a stoichiometric system. Although a correlation between E_{form} and the Li/Si ratio might be expected, none is observed. In addition, it was suggested in [45] that Li diffusivities might correlate with compound formation energies. However, for the larger set of crystal structures considered here, E_{form} of defects do not correlate with those of the compounds; see table S21 of the supporting information for the respective values. Among the structural properties considered, only the complexity of the crystal structure actually correlates with the lowest defect formation energy, see figure 5.

The crystIT script [89] was used to calculate complexity parameters of the crystal structures based on concepts proposed by Krivovichev in 2014 [90], extended by Hornfeck in 2020 [91], and further developed by Krivovichev *et al* in 2022 [92]. These information-theoretical concepts are based on applying Shannon entropy to crystal structures, and three complexity measures have been defined: combinatorial, coordinational, and configurational complexity. To evaluate the information content of

Li_xSi_y crystal structures, we use the volume-normalized configurational complexity, $I_{\mathrm{conf,dens}}$. This parameter, which includes both combinatorial and coordinational complexity, is normalized to the unit cell volume and thus has units of bits per Å^3.

Figure 5 shows the lowest formation energies of Frenkel defects and metastable structures in Li_xSi_y, plotted against $I_{\mathrm{conf,dens}}$ of the crystal structures. It is observed that E_{form} decreases roughly linearly with increasing complexity density between 0.1 and 0.5 bits/Å^3, and then plateaus at 0.01 eV for the two most complex structures above 0.5 bits/Å^3. Note that this plateau arises from the existence of metastable structures in β-$Li_{15}Si_4$ and model B of $Li_{4.11}Si$, whereas Frenkel defects remain higher in energy.

Although a detailed investigation into the underlying causes of this nonobvious correlation is beyond the scope of this study, we propose two qualitative considerations. First, high-complexity superstructures of Li_7Si_3 and $Li_{4.11}Si$ were constructed to resolve partial occupancies of crystallographic Li sites, resulting in intrinsic vacancies at those sites that remain unoccupied. These vacancies provide low-energy sites for Frenkel defect formation in Li_7Si_3 and for metastable structure formation $Li_{4.11}Si$ (model B). This fairly direct correlation between high complexity and low defect formation energy holds for only two of the compounds. Second, one might argue that the lower a crystal structure's complexity, the more 'perfect' it is—and the more energy is required to introduce a defect into its more perfect lattice. While this idea is purely qualitative and grounded in chemical intuition, it may still guide future research.

In this work, we merely observe the correlation between defect formation energies in stoichiometric Li_xSi_y systems and crystal structure complexity, without offering a quantitative explanation. Based on this observation, we predict that $Li_{4.11}Si$ ($I_{\mathrm{conf,dens}} = 0.53$ bits/Å^3), described here by models A (Li_4Si) and B ($Li_{4.125}Si$), exhibits a low defect formation energy ($\lessapprox 0.20$ eV), preferentially of a metastable structure rather than a Frenkel defect. We again note that $I_{\mathrm{conf,dens}}$ does not correlate with the Li/Si ratio. The most obvious examples are $Li_{15}Si_4$ and its β-phase, which share the same Li/Si ratio but have vastly different configurational complexity densities of 0.12 and 0.57 bits/Å^3, respectively. Therefore, we conclude that crystal structure complexity is a better predictor of defect formation energy, at least in the Li–Si system, and we want to draw attention to this parameter in materials design.

Experimental standard entropies for seven Li_xSi_y compounds are presented in [93]: one measured directly in that work, and six drawn from previous studies. These measured thermodynamic entropy values correlate fairly well with the information theoretical values of $I_{\mathrm{conf,dens}}$ (see supporting information, table S21), considering additional experimental entropy contributions (electronic, vibrational, etc), further validating the complexity concept applied here. The main drawback of our complexity analysis is its small dataset of only 14 data points, however, the Li–Si phase diagram contains no additional compounds. Thus, it would be valuable for future studies to evaluate the observed correlation in a broader range of compound classes.

4. Conclusions

By combining AIMD simulations with NEB calculations, we have, to our knowledge for the first time, thoroughly investigated several types of isovalent extrinsic point defects in crystalline lithium-silicon compounds Li_xSi_y in the context of Li diffusion. We have analyzed the impact of substitutional Na and Ge atoms as well as Na interstitials on the key migration pathways in Li_1Si_1, $Li_{12}Si_7$, $Li_{13}Si_4$, and $Li_{15}Si_4$. Since Na interstitials were found to be unstable, it is concluded that larger size atoms are likely found as substitutional atoms. Both substitutional Na and Ge atoms do not affect Li diffusivities or diffusion anisotropies substantially. Thus, there is no diffusion observed in Li_1Si_1 and $Li_{15}Si_4$, but fast ionic conduction in $Li_{12}Si_7$ and $Li_{13}Si_4$, as known from previous work. The local effect of substitutional atoms on nearby Li diffusion paths is of the order of a 10% increase in migration barriers, that can be attributed to larger atomic radii of Na and Ge causing local lattice strain. Overall lattice stiffness as measured by elastic moduli tends to decrease with substitutional Na and Ge atoms. Although this softening is more pronounced for substitution on the Li sublattice, it is correlated with a non-local less than 10% lowering of diffusion barriers in both cases. Substitutional Na formation energies are significantly higher than for Ge, probably due to larger local strain. As with Li, Na mobility strongly depends on the lattice site, with migration energies of Na atoms being about 30% higher than those of Li atoms. Overall, the effects on Li migration are rather minor. Transferring these findings to Si anodes under the assumption of similar effects in amorphous Li_xSi, actively doping either the cationic or anionic sublattice isovalently does not appear useful to promote diffusion, but on the other hand impurities are not expected to inhibit it.

We have further detected an inverse correlation between crystal structure complexity and the formation energies of Frenkel defects and metastable structures in stoichiometric Li_xSi_y systems. This finding draws attention to the application of complexity parameters as predictive descriptors in materials science. Since Li diffusivity has been studied exhaustively in crystalline lithium silicides by now, we proceed to investigate amorphous structures, with the ultimate aim to construct a multiscale model for simulation of Li mobility in both crystalline and amorphous systems.

Data availability statement

The data that support the findings of this study are openly available at the following URL/DOI: https://doi.org/10.5281/zenodo.15670547.

Li Diffusion SiX-LiY available at https://doi.org/10.1088/2515-7655/ae175e/data1.

Acknowledgments

This Project was funded by the Deutsche Forschungsgemeinschaft, Project ID 435886714.

ORCID iDs

Christoph Kirsch 0000-0002-4244-8888
Daniel Sebastiani 0000-0003-2240-3938

References

[1] Tarascon J and Armand M 2001 Issues and challenges facing rechargeable lithium batteries *Nature* **414** 359
[2] Armand M and Tarascon J 2008 Building better batteries *Nature* **451** 652
[3] Kasavajjula U, Wang C and Appleby A J 2007 Nano- and bulk-silicon-based insertion anodes for lithium-ion secondary cells *J. Power Sources* **163** 1003
[4] Huggins R A 2009 *Advanced Batteries - Materials Science Aspects* 1st edn (Springer)
[5] Schweidler S, deBiasi L, Schiele A, Hartmann P, Brezesinski J and Janek T 2018 Volume changes of graphite anodes revisited: a combined operando X-ray diffraction and *in situ* pressure analysis study *J. Phys. Chem. C* **122** 8829
[6] Limthongkul P, Jang Y, Dudney N J and Chiang Y 2003 Electrochemically-driven solid-state amorphization in lithium-silicon alloys and implications for lithium storage *Acta Mater.* **51** 1103
[7] Obrovac M N and Christensen L 2004 Structural changes in silicon anodes during lithium insertion/extraction *Electrochem. Solid-State Lett.* **7** A93
[8] Li J and Dahn J R 2007 An in situ x-ray diffraction study of the reaction of Li with crystalline Si *J. Electrochem. Soc.* **154** A156
[9] Zeilinger M, Baran V, van Wüllen L, Häussermann U and Fässler T F 2013 Stabilizing the phase $Li_{15}Si_4$ through lithium–aluminum substitution in $Li_{15-x}Al_xSi_4$ ($0.4 < x < 0.8$) — single crystal X-ray structure determination of $Li_{15}Si_4$ and $Li_{14.37}Al_{0.63}Si_4$ *Chem. Mater.* **25** 4113
[10] Stearns L A, Gryko J, Diefenbacher J, Ramachandran G K and McMillan P F 2003 Lithium monosilicide (LiSi), a low-dimensional silicon-based material prepared by high pressure synthesis: NMR and vibrational spectroscopy and electrical properties characterization *J. Solid State Chem.* **173** 251
[11] Nesper R, von Schnering H G and Curda J 1986 $Li_{12}Si_7$, eine Verbindung mit trigonal-planaren Si_4-Clustern und isometrischen Si_5-Ringen *Chem. Ber.* **119** 3576
[12] Barvík I 1983 To the magnetic properties of $Li_{2.33}Si$ *Czech. J. Phys. B* **33** 1338–46
[13] Zeilinger M and Fässler T F 2013 Revision of the $Li_{13}Si_4$ structure *Acta Cryst. E* **69** i81
[14] Zeng Z, Zeng Q, Liu N, Oganov A R, Zeng Q, Cui Y and Mao W L 2015 A novel phase of $Li_{15}Si_4$ synthesized under pressure *Adv. Energy Mater.* **5** 1500214
[15] Zeilinger M, Kurylyshyn I M, Häussermann U and Fässler T F 2013 Revision of the Li–Si phase diagram: discovery and single-crystal X-ray structure determination of the high-temperature phase $Li_{4.11}Si$ *Chem. Mater.* **25** 4623
[16] Nesper R and von Schnering H G 1987 $Li_{21}Si_5$, a Zintl phase as well as a Hume-Rothery phase *J. Solid State Chem.* **70** 48
[17] Zeilinger M, Benson D, Häussermann U and Fässler T F 2013 Single crystal growth and thermodynamic stability of $Li_{17}Si_4$ *Chem. Mater.* **25** 1960
[18] Gladyshevskii E, Oleksiv G and Kripyakevich P I 1964 New examples of the structural type $Li_{22}Pb_5$ *Kristallografiya* **9** 338
[19] Nesper R 1990 Structure and chemical bonding in Zintl-phases containing lithium *Prog. Solid State Chem.* **20** 1
[20] Chevrier V, Zwanziger J and Dahn J 2010 First principles study of Li–Si crystalline phases: charge transfer, electronic structure and lattice vibrations *J. Alloys Compd.* **496** 25
[21] Mehrer H 2007 *Diffusion in Solids - Fundamentals, Methods, Materials, Diffusion-Controlled Processes* 1st edn (Springer)
[22] Ding N, Xu J, Yao Y, Wegner G, Fang X, Chen C and Lieberwirth I 2009 Determination of the diffusion coefficient of lithium ions in nano-Si *Solid State Ion.* **180** 222
[23] Wang Z *et al* 2013 Electron-rich driven electrochemical solid-state amorphization in Li–Si alloys *Nano Lett.* **13** 4511
[24] Gu M, Wang Z, Connell J G, Perea D E, Lauhon L J, Gao F and Wang C 2013 Electronic origin for the phase transition from amorphous Li_xSi to crystalline $Li_{15}Si_4$ *ACS Nano* **7** 6303
[25] Wen C J and Huggins R A 1981 Chemical diffusion in intermediate phases in the lithium-silicon system *J. Solid State Chem.* **37** 271
[26] Dupke S, Langer T, Pöttgen R, Winter M and Eckert H 2012 Structural and dynamic characterization of $Li_{12}Si_7$ and $Li_{12}Ge_7$ using solid state NMR *Solid State Nucl. Magn. Reson.* **42** 17
[27] Dupke S, Langer T, Pöttgen R, Winter M, Passerini S and Eckert H 2012 Structural characterization of the lithium silicides $Li_{15}Si_4$, $Li_{13}Si_4$, and Li_7Si_3 using solid state NMR *Phys. Chem. Chem. Phys.* **14** 6496
[28] Kuhn A, Sreeraj P, Pöttgen R, Wiemhöfer H-D, Wilkening M and Heitjans P 2011 Li ion diffusion in the anode material $Li_{12}Si_7$: ultrafast quasi-1D diffusion and two distinct fast 3D jump processes separately revealed by ^{7}Li NMR relaxometry *J. Am. Chem. Soc.* **133** 11018

[29] Kuhn A, Dupke S, Kunze M, Puravankara S, Langer T, Pöttgen R, Winter M, Wiemhöfer H-D, Eckert H and Heitjans P 2014 Insight into the Li ion dynamics in $Li_{12}Si_7$: combining field gradient nuclear magnetic resonance, one- and two-dimensional magic-angle spinning nuclear magnetic resonance and nuclear magnetic resonance relaxometry *J. Phys. Chem. C* **118** 28350

[30] Tritsaris G A, Zhao K, Okeke O U and Kaxiras E 2012 Diffusion of lithium in bulk amorphous silicon: a theoretical study *J. Phys. Chem. C* **116** 22212

[31] Yan X, Gouissem A and Sharma P 2015 Atomistic insights into Li-ion diffusion in amorphous silicon *Mech. Mater.* **91** 306

[32] Wan W, Zhang Q, Cui Y and Wang E 2010 First principles study of lithium insertion in bulk silicon *J. Phys.: Condens. Matter* **22** 415501

[33] Kim H, Kweon K E, Chou C-Y, Ekerdt J G and Hwang G S 2010 On the nature and behavior of Li atoms in Si: a first principles study *J. Phys. Chem. C* **114** 17942

[34] Haldar P and Chatterjee A 2014 Nudged-elastic band study of lithium diffusion in bulk silicon in the presence of strain *Energy Proc.* **54** 310

[35] Malyi O I, Tan T L and Manzhos S 2013 A comparative computational study of structures, diffusion and dopant interactions between Li and Na insertion into Si *Appl. Phys. Express* **6** 027301

[36] Chou C-Y, Kim H and Hwang G S 2011 A comparative first-principles study of the structure, energetics and properties of Li–M (M = Si, Ge, Sn) alloys *J. Phys. Chem. C* **115** 20018

[37] Kim H, Chou C-Y, Ekerdt J G and Hwang G S 2011 Structure and properties of Li-Si alloys: a first-principles study *J. Phys. Chem. C* **115** 2514

[38] Wang G, Xu B, Shi J, Wu M, Su H and Ouyang C 2019 New insights into Li diffusion in Li–Si alloys for Si anode materials: role of Si microstructures *Nanoscale* **11** 14042

[39] Johari P, Qi Y and Shenoy V B 2011 The mixing mechanism during lithiation of Si negative electrode in Li-ion batteries: an ab initio molecular dynamics study *Nano Lett.* **11** 5494

[40] Wang Z, Su Q, Deng H and Fu Y 2015 Composition dependence of lithium diffusion in lithium silicide: a density functional theory study *ChemElectroChem* **2** 1292

[41] Yao H R, Wang Z Q, Wu M S, Liu G, Lei X L, Xu B, Le J X and Ouyang C Y 2014 Lithium ion migration in Li-Si alloys: from first principles studies *Int. J. Electrochem. Sci.* **9** 1854

[42] Shi J, Wang Z and Fu Y 2015 Atomistic study of lithium ion dynamics in $Li_{12}Si_7$ *Electrochim. Acta* **186** 71

[43] Gruber T, Bahmann S and Kortus J 2016 Metastable structure of $Li_{13}Si_4$ *Phys. Rev. B* **93** 144104

[44] Kirsch C, Dreßler C and Sebastiani D 2022 Atomistic diffusion pathways of lithium ions in crystalline lithium silicides from ab initio molecular dynamics simulations *J. Phys. Chem. C* **126** 12136

[45] Kirsch C, Dreßler C and Sebastiani D 2025 Li^+ diffusion in crystalline lithium silicides: influence of intrinsic point defects *J. Phys. Energy* **7** 025003

[46] Moon J, Lee B, Cho M and Cho K 2016 Ab initio and kinetic Monte Carlo study of lithium diffusion in LiSi, $Li_{12}Si_7$, $Li_{13}Si_5$ and $Li_{15}Si_4$ *J. Power Sources* **328** 558

[47] Wang Z, Su Q, Deng H, He W, Lin J and Fu Y Q 2014 Modelling and simulation of electron-rich effect on Li diffusion in group IVA elements (Si, Ge and Sn) for Li ion batteries *J. Mater. Chem. A* **2** 13976

[48] Momma K and Izumi F 2011 *VESTA3* for three-dimensional visualization of crystal, volumetric and morphology data *J. Appl. Crystallogr.* **44** 1272

[49] Humphrey W, Dalke A and Schulten K 1996 VMD: visual molecular dynamics *J. Mol. Graph.* **14** 33

[50] Jiang C, Maloy S and Srinivasan S 2008 A computational method to identify interstitial sites in complex materials *Scripta Mater.* **58** 739

[51] Hohenberg P and Kohn W 1964 Inhomogeneous electron gas *Phys. Rev.* **136** B864

[52] Kohn W and Sham L J 1965 Self-consistent equations including exchange and correlation effects *Phys. Rev.* **140** A1133

[53] Hutter J, Iannuzzi M, Schiffmann F and VandeVondele J 2014 CP2K: atomistic simulations of condensed matter systems *Wiley Interdiscip. Rev.-Comput. Mol. Sci.* **4** 15

[54] Kühne T D *et al* 2020 CP2K: an electronic structure and molecular dynamics software package - Quickstep: efficient and accurate electronic structure calculations *J. Chem. Phys.* **152** 194103

[55] VandeVondele J, Krack M, Mohamed F, Parrinello M, Chassaing T and Hutter J 2005 Quickstep: fast and accurate density functional calculations using a mixed Gaussian and plane waves approach *Comput. Phys. Commun.* **167** 103

[56] Lippert G, Hutter J and Parrinello M 1997 A hybrid Gaussian and plane wave density functional scheme *Mol. Phys.* **92** 477

[57] VandeVondele J and Hutter J 2007 Gaussian basis sets for accurate calculations on molecular systems in gas and condensed phases *J. Chem. Phys.* **127** 114105

[58] Goedecker S, Teter M and Hutter J 1996 Separable dual-space Gaussian pseudopotentials *Phys. Rev. B* **54** 1703

[59] Hartwigsen C, Goedecker S and Hutter J 1998 Relativistic separable dual-space Gaussian pseudopotentials from H to Rn *Phys. Rev. B* **58** 3641

[60] Krack M 2005 Pseudopotentials for H to Kr optimized for gradient-corrected exchange-correlation functionals *Theor. Chem. Acc.* **114** 145

[61] Perdew J P, Burke K and Ernzerhof M 1996 Generalized gradient approximation made simple *Phys. Rev. Lett.* **77** 3865

[62] Perdew J P, Burke K and Ernzerhof M 1997 Generalized gradient approximation made simple [Phys. Rev. Lett. 77, 3865 (1996)] *Phys. Rev. Lett.* **78** 1396

[63] Grimme S, Antony J, Ehrlich S and Krieg H 2010 A consistent and accurate ab initio parametrization of density functional dispersion correction (DFT-D) for the 94 elements H-Pu *J. Chem. Phys.* **132** 154104

[64] Freysoldt C, Grabowski B, Hickel T, Neugebauer J, Kresse G, Janotti A and Vande Walle C G 2014 First-principles calculations for point defects in solids *Rev. Mod. Phys.* **86** 253

[65] Broberg D *et al* 2023 High-throughput calculations of charged point defect properties with semi-local density functional theory—performance benchmarks for materials screening applications *npj Comput. Mater.* **9** 72

[66] Gao W, Abtew T A, Cai T, Sun Y-Y, Zhang S and Zhang P 2016 On the applicability of hybrid functionals for predicting fundamental properties of metals *Solid State Commun.* **234–235** 10–13

[67] Stroppa A, Termentzidis K, Paier J, Kresse G and Hafner J 2007 Co adsorption on metal surfaces: a hybrid functional study with plane-wave basis set *Phys. Rev. B* **76** 195440

[68] Mermin N D 1965 Thermal properties of the inhomogeneous electron gas *Phys. Rev.* **137** A1441

[69] Broyden C G 1965 A class of methods for solving nonlinear simultaneous equations *Math. Comp.* **19** 577

[70] Broyden C G 1970 The convergence of a class of double-rank minimization algorithms 1. general considerations *IMA J. Appl. Math.* **6** 76

[71] Fletcher R 1970 A new approach to variable metric algorithms *Comput. J.* **13** 317

[72] Goldfarb D 1970 A family of variable-metric methods derived by variational means *Math. Comp.* **24** 23

[73] Shanno D F 1970 Conditioning of quasi-Newton methods for function minimization *Math. Comp.* **24** 647

[74] Monkhorst H J and Pack J D 1976 Special points for Brillouin-zone integrations *Phys. Rev. B* **13** 5188

[75] deJong M *et al* 2015 Charting the complete elastic properties of inorganic crystalline compounds *Sci. Data* **2** 1

[76] Nosé S 1984 A molecular dynamics method for simulations in the canonical ensemble *Mol. Phys.* **52** 255

[77] Nosé S 1984 A unified formulation of the constant temperature molecular dynamics methods *J. Chem. Phys.* **81** 511

[78] Henkelman G, Uberuaga B P and Jónsson H 2000 A climbing image nudged elastic band method for finding saddle points and minimum energy paths *J. Chem. Phys.* **113** 9901

[79] Mills G, Jónsson H 1994 Quantum and thermal effects in H_2 dissociative adsorption: evaluation of free energy barriers in multidimensional quantum systems *Phys. Rev. Lett.* **72** 1124

[80] Mills G, Jónsson H and Schenter G K 1995 Reversible work transition state theory: application to dissociative adsorption of hydrogen *Surf. Sci.* **324** 305

[81] Berne B J, Ciccotti G and Coker D F 1998 *Classical and Quantum Dynamics in Condensed Phase Simulations* 1st edn (World Scientific)

[82] Henkelman G, Jónsson H 2000 Improved tangent estimate in the nudged elastic band method for finding minimum energy paths and saddle points *J. Chem. Phys.* **113** 9978

[83] Persson K, Sethuraman V A, Hardwick L J, Hinuma Y, Meng Y S, vander Ven A, Srinivasan V, Kostecki R and Ceder G 2010 Lithium diffusion in graphitic carbon *J. Phys. Chem. Lett.* **1** 1176

[84] Mo Y, Ong S P and Ceder G 2012 First principles study of the $Li_{10}GeP_2S_{12}$ lithium super ionic conductor material *Chem. Mater.* **24** 15

[85] Boey S and Bacon D 1986 Deformation of polycrystalline graphite under pressure *Carbon* **24** 557

[86] Deng Z, Wang Z, Chu I-H, Luo J and Ong S P 2015 Elastic properties of alkali superionic conductor electrolytes from first principles calculations *J. Electrochem. Soc.* **163** A67

[87] Varotsos P, Ludwig W and Alexopoulos K 1978 Calculation of the formation volume of vacancies in solids *Phys. Rev. B* **18** 2683

[88] Chevrier V L, Zwanziger J W and Dahn J R 2009 First principles studies of silicon as a negative electrode material for lithium-ion batteries *Can. J. Phys.* **87** 625

[89] Kaußler C and Kieslich G 2021 crystIT: complexity and configurational entropy of crystal structures via information theory *J. Appl. Crystallogr.* **54** 306

[90] Krivovichev S V 2014 Which inorganic structures are the most complex? *Angew. Chem. Int. Ed.* **53** 654

[91] Hornfeck W 2020 On an extension of Krivovichev's complexity measures *Acta Crystallogr. A* **76** 534

[92] Krivovichev S V *et al* 2022 Structural and chemical complexity of minerals: an update *Mineral. Mag.* **86** 183–204

[93] Taubert F, Seidel J, Hüttl R, Bobnar M, Gumeniuk R and Mertens F 2018 The heat capacity and entropy of the metastable lithium silicide $Li_{15}Si_4$ in the temperature range (2–615) K *J. Chem. Thermodyn.* **116** 323